



A vortex approach for unsteady insect flight analysis in 2D

M. Denda , Pruthvi K. Jujjavarapu  and Brandon C. Jones 

Mechanical and Aerospace Engineering Department, Rutgers University, Piscataway, NJ, USA

ABSTRACT

This paper considers 2D insect wing motion in which the flow field does not change in the out-of-plane direction. When modelling complex phenomena, simpler, but not overly simple, analysis techniques become imperative. We achieve the balance of simplicity and accuracy by a technique based on the vortex. The wing is represented by its chord, described by a line in 2D. During the unsteady flapping, a time-dependent circulation pattern is developed over the wing, modelled by the distribution of discrete line vortices. The magnitudes of the bound vortices on the wing are determined by the non-penetration condition. Two vortices at the wing's leading and trailing edges are shed. The velocity is determined by the bound and wake vortices using 2D Biot–Savart law, which is also used to convect wake vortices. The entire cycle is repeated as the time progresses. While establishing a simple affordable numerical method for flapping wing analysis and highlighting its remarkable performance, the limitation of the method is delineated and recommendations made in comparison with more accurate solutions obtained by a Navier–Stokes solver. This will ensure the proper use of the method and avoid its misuse in the unsteady aerodynamics analysis.

ARTICLE HISTORY

Received 14 October 2015
Accepted 6 June 2016

KEYWORDS


Vortex method; quick 2D unsteady flow solver; vortex shedding; leading and trailing edges; insect flight dynamics

1. Introduction

The study of insect flight has been a relatively new area of research motivated by the emerging MAV (micro aerial vehicle) technology rather than for its own interest. In the spirit of biomimicry, learning from nature helps design engineers come up with new and effective flapping mechanisms used by MAVs. Insects move their wings using the muscles in the thorax. Unlike birds and bats, which are equipped with muscles and bones built into the wings, insect wings are free from these, making them simpler and lighter. This is the major reason we study insects, rather than other flying animals, for the inspiration of very light weight MAV design.

The major thrust in computational fluid dynamics has been in the steady-state analysis, in which the fluid field remains constant. The steady-state assumption serves the majority of the analysis for the flight of fixed-wing aeroplane. With

CONTACT M. Denda  denda@rutgers.edu

 Supplemental material for this article can be accessed here. [<http://dx.doi.org/10.1080/17797179.2016.1199236>]

the advent of MAVs that use flapping, the importance of reliable computational techniques for unsteady analysis has been sought. Many have resorted to the extension of the existing CFD techniques, typically the finite volume method (Liu & Aono, 2009), into the unsteady domain. Some have invented and developed new techniques suitable for the unsteady problem, such as the immersed boundary method (Wang, 2005). Common to most of them is the assumption of viscous flow leading to some form of Navier–Stokes equation solvers. This is because, for low Reynolds number flow, such as in most of the flapping phenomena, the effect of viscosity is prevalent. This makes the solution expensive and restricts the range of solvable problems narrow.

When modelling complex phenomena, such as the flapping flight, simpler analysis techniques become imperative. However, they cannot be overly simple such as the quasi-static approximation that misses the essence of the unsteady phenomena. The balance is achieved by techniques based on the vortex. Quite a few variations of methods using the vortex exist (Katz & Plotkin, 2001; Lewis, 1991), but they are all equivalent in the sense that the influence function based on Biot–Savart formula is used, leading to the Boundary Element-like approach rather than the Finite Element- or Finite Volume-like domain approach. When the fluid domain is concerned, the former, unlike the latter, does not require meshing of the domain, leading to less data intensive approach. One of the basic ideas of this paper comes from (Ansari et al., 2006a, 2006b; von Kármán & Sears, 1938 and McCune & Tavares, 1993), in which the discrete vortex distribution along the aerofoil and in the wake was used for the solution of unsteady 2D ideal flow problems. The most remarkable feature, initiated by von Kármán & Sears and inherited by the rest of the authors listed above, is the use of impulses (linear and angular) and their derivatives to calculate the force and moment on the aerofoil. This approach is simpler and more elegant than the alternative approach using the unsteady Bernoulli equation. However, while the latter can provide the force and moment locally for any point over the wing, the former can only give them on the wing as a whole. This impulse approach is suitable for rigid wings as in this paper. If we need to calculate the local deformation on the wing, the Bernoulli equation must be used.

The approach outlined above is also inspired by the discrete vortex method of Belotserkovsky (Belotserkovsky et al., 1993; Belotserkovsky & Lifanov, 2003), who pioneered the solution procedure of the unsteady viscous problems using the discrete vortices coupled with the boundary layer analysis to deal with the viscous and turbulent unsteady problems in the framework of potential flow theory. In applying this approach to the insect flight analysis, the entire domain is divided into three regions: thin wing, viscous boundary layer around the wing and the surrounding infinite inviscid fluid. The boundary layer, in turn, is modelled by an array of discrete vortices bound on the wing. Unlike finite thickness wings, which were the main focus of Belotserkovsky, there is no need to perform the viscous boundary layer analysis to find out the flow separation points along the

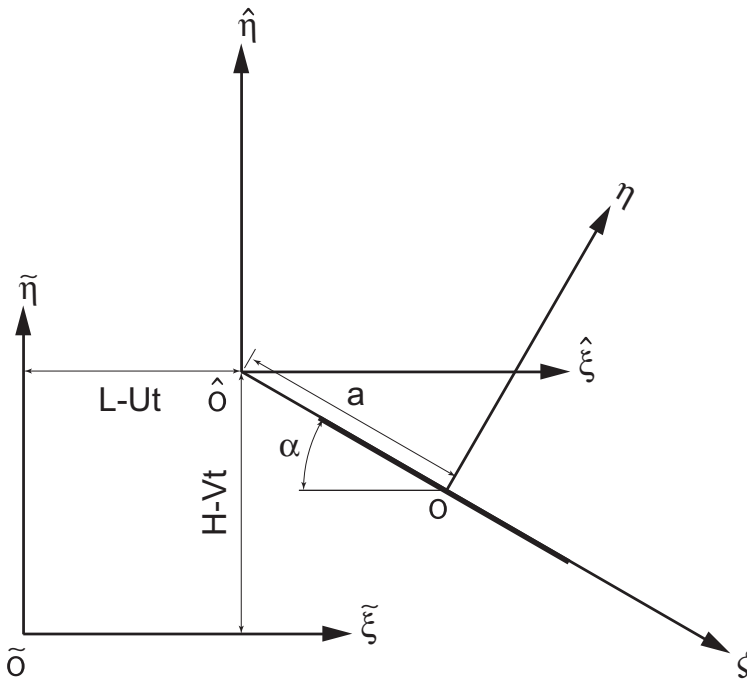


Figure 1. Space-fixed ($\tilde{O} - \tilde{\xi} \tilde{\eta}$), wing-fixed ($O - \xi \eta$) and wing-translating ($\hat{O} - \hat{\xi} \hat{\eta}$) coordinate systems.

thin wing, at high angles of attack, since these points are known to be the leading edge (LE) and trailing edge (TE) of the wing. While most of the vortex-based methods use Kutta condition for the shedding of edge vortices, it is not enforced at all. Rather, vortices are regularly shed from the LE and TE of the wing. Since the density of the bound vortex at these edges is reduced to zero immediately after shedding, it effectively satisfies the Kutta condition at these points. Comparison of the current shedding approach to the traditional way of enforcing the Kutta condition gives the outcome in favour of the former. Thus, the flow separation is modelled by the shedding of vortices from these two edges. Once these vortices are shed they become wake vortices which convect with the fluid velocity. This procedure is applicable regardless of the values of the Reynolds number; for large Reynolds numbers, the number of vortices increases and the problem of turbulence is reduced to the many-wake-vortices problem in the inviscid fluid.

2. 2D motion of flapping insect wing

2.1. Coordinate systems

Three coordinate systems are employed to describe the local and global positions of the wing as shown in Figure 1. The wing, represented by a solid line in the figure, is assumed to be thin and rigid. The original infinitely long (in the span direction) wing is represented by its intersection with the 2D plane. The shape

of this cross section represents the chord of the wing, which is represented either locally by the wing-fixed system $O - \xi\eta$ or globally space-fixed system $\tilde{O} - \tilde{\xi}\tilde{\eta}$. The geometry of the wing is described by a set of (ξ, η) values, which remains constant; its global position is described by the corresponding set $(\tilde{\xi}, \tilde{\eta})$, which varies during the motion of the wing. The wing undergoes two translational (lunge and heave) and one rotational (pitch) motions. The origin of the third coordinate system, $\hat{O} - \hat{\xi}\hat{\eta}$, is placed at the centre of rotation of the wing, which could coincide with the coordinate origin O of the wing-fixed system or, in general, located at a distance a along the negative ξ axis, defining the rotational offset. In addition the axes, $\hat{\xi}$ and $\hat{\eta}$, of this last system is parallel to the global $\tilde{\xi}$ and $\tilde{\eta}$, respectively. While the wing-fixed system rotates and translates with the wing, the system $\hat{O} - \hat{\xi}\hat{\eta}$ only translates and is called the wing-translating system.

2.2. Wing position

The typical insect flight motion in 3D consists of three components of rotation, roll, pitch and yaw, in addition to another three translational components. For insects with a long wing span length, such as dragonflies, damselflies and crane flies, the flow in the middle of the span approximately remains constant in the span direction. This justifies the 2D modelling of the wing motion provided the right and left wing pitch and roll are symmetric and the yaw is absent. This paper considers such a class of 2D wing motions, in which the flow field does not change in the out-of-plane direction. In 2D the pitch remains as original in 3D but the roll, in 2D, is recast as a translational motion consisting of the heave (up and down) and lunge (forward and back) components. These motions are added to the genuine translational motion of the insect.

While the rolling of a finite length insect wing, either right or left wing, in 3D is described by the rotation around the body axis, it is represented, in 2D, by a translational motion of an infinitely long wing along the stroke line. Figure 2 shows the projection of the stroke plane with the 2D plane as a straight inclined line (stroke line) with the slope, β , measured positive counterclockwise from the horizontal line. This angle is called the stroke line angle as shown in Figure 2. This translational motion is decomposed into the horizontal (lunge), L , and vertical (heave), H , components. The wing undergoes another kind of rotation around the wing span, which is called the pitch denoted by α . The forward pitch, in the down-stroke direction with $\alpha < 0$, is called the pronation and the backward pitch, in the direction of the up-stroke with $\alpha > 0$, is called the supination.

Since the lunge and heave in 2D originate from the rolling in 3D, it is convenient to introduce a hypothetical 3D wing, of the same chord length as the 2D wing but with a finite span length l . Also introduce the upper and lower stroke angles, ϕ_T and ϕ_B , respectively, undergone by this 3D wing as shown in Figure 3. These three quantities are taken from the actual insect flight motions and can be used to specify the extent of the stroke line, which is obtained by

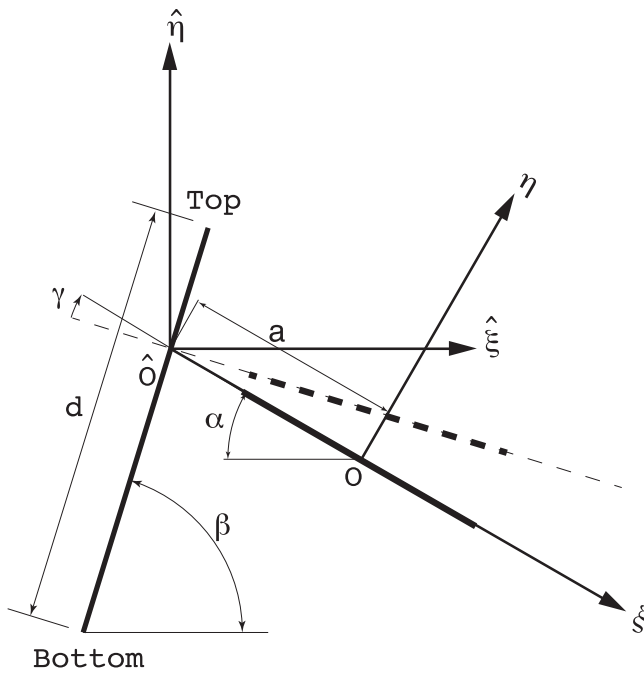


Figure 2. Stroke line of length d and angle β . Pitch γ and attack angle α .

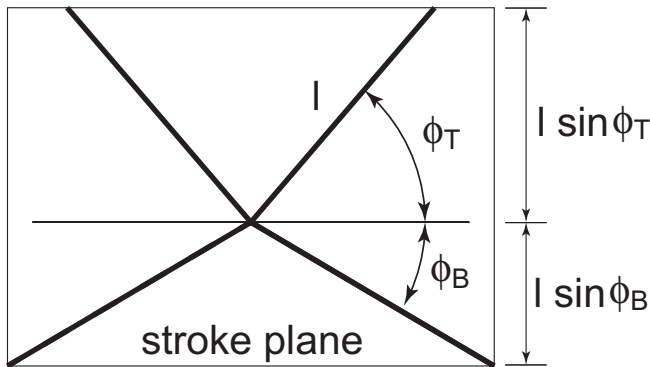


Figure 3. The stroke plane view of the wing's topmost (ϕ_T) and bottommost (ϕ_B) positions. Wings on left and right sides are shown, each at the extreme positions.

projecting the 3D wing geometry into 2D. The time variation of the lunge and heave is expressed using the sinusoidal functions.

The pitch motion, in principle, is assumed to take place at the extremes of each stroke as a sudden rotation. The pronation occurs at the top of the stroke by pitching the wing in the downward direction, while the supination is induced at the bottom of the stroke in the upward direction. However, pitch motions of some insects occur before reaching the top or bottom stroke point (advanced pitch) and others show the pitch after (delayed pitch). Also notice that most insects

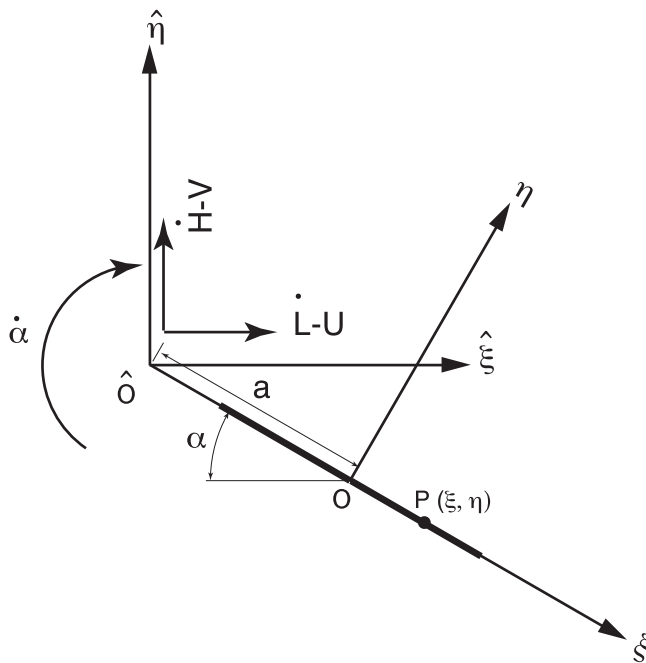


Figure 4. Translational and rotational velocities of the wing-translating and wing-fixed coordinate systems.

do not have the capability to pitch instantaneously and the rotation is smoothed out. Our pitch motion reflects this fact and a smoothed out step function is used.

The effect of the ambient air velocity, (U, V) , is incorporated by moving the wing itself in the direction opposite to the air velocity under zero ambient velocity. We assume the constant air velocity and the total translational motion of the wing are obtained by superposing the contributions from the flapping motion and the air velocity to give $(L - Ut, H - Vt)$, where t is the time.

All the wing position variables introduced are displayed in Figure 1. Here, $(L - Ut, H - Vt)$ gives the coordinates of the wing-translating system origin \hat{O} , α gives the slope of the ξ -axis of the wing-fixed system and a is the distance of the origins of the wing-fixed and wing-translating systems. The details of the wing motion are given in Appendix 1.

2.3. Wing velocity

Figure 4 shows the translational velocity, $(\dot{L} - U, \dot{H} - V)$, of the wing-translating system origin and the superposed translational $(\dot{L} - U, \dot{H} - V)$ and rotational $(\dot{\alpha})$ velocities of the wing-fixed system origin. The centre of rotation is located at the origin \hat{O} of the wing-translating system. Given these wing velocity parameters, we can calculate the velocity of an arbitrary point $P = (\xi, \eta)$ on the wing, which, in the wing-translating system, is given by the coordinates $(\hat{\xi}, \hat{\eta})$. The linear velocity resulting from the rotation of point \hat{P} around \hat{O} is given by the cross product

$$\mathbf{r}_{\hat{O}\hat{P}} \times (-\dot{\alpha}\mathbf{k}), \quad (1)$$

where \mathbf{k} is the out-of-plane unit vector.

In 2D, it is convenient to use complex variables. Let $\hat{\zeta} = \hat{\xi} + i\hat{\eta}$ and $\zeta = \xi + i\eta$ to describe complex-valued positions of the wing in the wing-translating and wing-fixed systems, respectively. They are related by

$$\hat{\zeta} = (a + \zeta)e^{-i\alpha}.$$

The complex-valued velocity (1) is given by

$$[V_{\hat{\xi}} + iV_{\hat{\eta}}]_{rot} = \dot{\alpha}\hat{\zeta}e^{-i\pi/2} = -i\dot{\alpha}\hat{\zeta}, \quad (2)$$

where $e^{-i\pi/2}$ rotates the complex position vector $\hat{\zeta}$ by 90° in the clockwise direction. Combined with the complex-valued velocity of the origin \hat{O} ,

$$[V_{\hat{\xi}} + iV_{\hat{\eta}}]_{trans} = \dot{L} - U + i(\dot{H} - V),$$

we get the total velocity of the point \hat{P} (or equivalently P) on the wing

$$V_{\hat{\zeta}} = V_{\hat{\xi}} + iV_{\hat{\eta}} = (\dot{L} - U) + i(\dot{H} - V) - i\dot{\alpha}\hat{\zeta} = (\dot{L} - U) + i(\dot{H} - V) - i\dot{\alpha}(a + \zeta)e^{-i\alpha}. \quad (3)$$

Since the wing-translating and space-fixed coordinate axes are parallel, this gives the space-fixed expression of the wing velocity

$$V_{\hat{\xi}} = V_{\xi} = \dot{L} - U + \dot{\alpha}(\eta \cos(\alpha) - (a + \xi) \sin(\alpha)), \quad (4)$$

$$V_{\hat{\eta}} = V_{\eta} = \dot{H} - V - \dot{\alpha}((a + \xi) \cos(\alpha) + \eta \sin(\alpha)). \quad (5)$$

in terms of the wing-fixed coordinates.

In this paper, the wing is assumed straight and the complex unit normal vector is given by

$$n = n_{\xi} + in_{\eta} = i \quad (6)$$

in the wing-fixed system and by

$$\tilde{n} = n_{\tilde{\xi}} + in_{\tilde{\eta}} = ne^{-i\alpha} = ie^{-i\alpha} \quad (7)$$

in the space-fixed system. The normal velocity of the wing is given, from (4)–(7), by

$$V^{\tilde{n}} = \Re(\tilde{V}_{\tilde{\zeta}}\tilde{n}) = V_{\tilde{\xi}}n_{\tilde{\xi}} + V_{\tilde{\eta}}n_{\tilde{\eta}}, \quad (8)$$

where $\Re()$ is the real part of a complex variable.

3. Vortex equations

3.1. Single vortex

The complex potential function (Sears, 2011) for a line vortex, with the circulation Γ and location $\tilde{\zeta}_0 = \tilde{\xi}_0 + i\tilde{\eta}_0$, is given by

$$\omega(\tilde{\zeta}) = -\frac{i\Gamma}{2\pi} \log(\tilde{\zeta} - \tilde{\zeta}_0), \quad (9)$$

where $\tilde{\zeta} = \tilde{\xi} + i\tilde{\eta}$ and $\tilde{\zeta}_0$ are complex position vectors in the space-fixed system. The circulation is positive counterclockwise. The conjugate of the complex velocity induced by this vortex at $\tilde{\zeta}$ is given by

$$\overline{v(\tilde{\zeta})} = \frac{d\omega}{d\tilde{\zeta}} = -\frac{i\Gamma}{2\pi} \frac{1}{\tilde{\zeta} - \tilde{\zeta}_0}, \quad (10)$$

where $v(\tilde{\zeta}) = v_{\tilde{\xi}} + iv_{\tilde{\eta}}$ and an overbar ($\bar{\cdot}$) indicates the complex conjugate.

When the distance between the observation and vortex points gets closer, the velocity at the observation point increases. This tendency becomes prevalent when the number of wake vortices increases. In order to avoid the excessive magnitude of the velocity, we introduce the Rankine vortex (Acheson, 1990) in Appendix 2.

All equations in Sections 3 and 4 are based on the formula (10). When the Rankine vortex model, as introduced in Appendix 2, is used, these equations need to be modified according to the Rankine vortex model Equations (B1) and (B2). Specifically, the velocity within the vortex core should be modified by Equation (B2), while the velocity outside the core remains as described by Equation (10) or (B1).

3.2. Discretisation of the wing

Introduce m vortices, Γ_j at $\tilde{\zeta}_{0j}$ ($j = 1, 2, \dots, m$) and $m - 1$ collocation points $\tilde{\zeta}_i$ ($i = 1, 2, \dots, m - 1$) on the wing. The vortices are placed at the LE and TE and in between. The spacing of the vortex points could be equidistant at the middle and gradually narrowed towards the edges. The number of vortices originally placed at an equal interval is m_0 ; as described in Appendix 3, this arrangement is refined by adding four more vortices at the two ends of the wing to give $m = m_0 + 4$. The collocation points are placed at the midpoints of vortex points.

3.3. Influence coefficients

The complex conjugate velocity at the wing collocation point $\tilde{\zeta}_i$ due to a vortex Γ_j at $\tilde{\zeta}_{0j}$ is given by

$$\bar{v}_{ij} = -\frac{i\Gamma_j}{2\pi} \frac{1}{\tilde{\zeta}_i - \tilde{\zeta}_{0j}}. \quad (11)$$

The normal component of this velocity at the collocation point is given, from Equation (8), by

$$v_{ij}^{\tilde{n}} = \Re(\bar{v}_{ij}\tilde{n}_i) = \frac{\Gamma_j}{2\pi} \Im\left(\frac{\tilde{n}_i}{\tilde{\zeta}_i - \tilde{\zeta}_{0j}}\right) \equiv V_{ij}^{\tilde{n}}\Gamma_j, \quad (12)$$

where \tilde{n}_i is given by Equation (7) at the collocation point, \Im is the imaginary part of a complex variable and

$$V_{ij}^{\tilde{n}} = \frac{1}{2\pi} \Im\left(\frac{\tilde{n}_i}{\tilde{\zeta}_i - \tilde{\zeta}_{0j}}\right), \quad (13)$$

is the influence coefficient.

4. System of equations for discrete vortices on the wing

4.1. Contribution from the bound vortices on the wing

Upon the initiation of the flapping motion, the vortices are developed on the wing and no wake is present. So the first set of equations consists only of the bound vortices. The more general equations including the bound and wake vortices are developed after this.

Add contributions from the entire discrete bound vortices on the wing to get the normal velocity component at the collocation point $\tilde{\zeta}_i$,

$$v_i^{\tilde{n}} = \sum_{j=1}^m V_{ij}^{\tilde{n}}\Gamma_j, \quad (14)$$

where $V_{ij}^{\tilde{n}}$ is given by Equation (13). The non-penetration condition requires that this normal velocity must be equal to the normal velocity of the wing, $V_i^{\tilde{n}}$, at each collocation point,

$$\sum_{j=1}^m V_{ij}^{\tilde{n}}\Gamma_j = V_i^{\tilde{n}}, \quad (15)$$

for collocation points $i = 1, 2, \dots, m - 1$. An additional equation, required to match the number of m unknowns, Γ_i , is given by the conservation of the vortices,

$$\sum_{j=1}^m \Gamma_j = 0, \quad (16)$$

which is the consequence of Helmholtz's third theorem (Katz & Plotkin, 2001; Ashley & Landahl, 1985) for the inviscid flow.

4.2. Contribution from the wake vortices

At each time step a pair of vortices, from the LE ($j = 1$) and TE ($j = m$), are shed from the wing such that during the p -th time period we have $2(p - 1)$ wake vortices,

$$\Gamma_1^{[1]}, \Gamma_m^{[1]}, \Gamma_1^{[2]}, \Gamma_m^{[2]}, \dots, \Gamma_1^{[p-1]}, \Gamma_m^{[p-1]}, \quad (17)$$

located at,

$$[p]\tilde{\zeta}_1^{[1]}, [p]\tilde{\zeta}_m^{[1]}, [p]\tilde{\zeta}_1^{[2]}, [p]\tilde{\zeta}_m^{[2]}, \dots, [p]\tilde{\zeta}_1^{[p-1]}, [p]\tilde{\zeta}_m^{[p-1]}, \quad (18)$$

where the pre-superscript $[p]()$ indicates the current step $[p]$ and the post-superscript $()^{[k]}$ ($k = 1, 2, \dots, p - 1$) indicates the originating time step. Notice that Γ 's do not have the pre-superscript since their values remain constant once the vortices are shed into the flow.

The complex conjugate velocity at the wing collocation point $\tilde{\zeta}_i$ due to the wake vortex pair $\Gamma_1^{[k]}$ and $\Gamma_m^{[k]}$ is given by

$$[p]\tilde{v}_{i[k]}^{\tilde{n}} = -\frac{i}{2\pi} \left(\frac{\Gamma_1^{[k]}}{\tilde{\zeta}_i - [p]\tilde{\zeta}_1^{[k]}} + \frac{\Gamma_m^{[k]}}{\tilde{\zeta}_i - [p]\tilde{\zeta}_m^{[k]}} \right), \quad (19)$$

for $k = 1, 2, \dots, p - 1$.

The normal component of this velocity at the collocation point $\tilde{\zeta}_i$ is given, from Equation (8), by

$$\begin{aligned} [p]v_{i[k]}^{\tilde{n}} &= \Re \left([p]\tilde{v}_{i[k]}^{\tilde{n}} \tilde{n}_i \right) = \frac{1}{2\pi} \left(\Gamma_1^{[k]} \Im \left(\frac{\tilde{n}_i}{\tilde{\zeta}_i - [p]\tilde{\zeta}_1^{[k]}} \right) + \Gamma_m^{[k]} \Im \left(\frac{\tilde{n}_i}{\tilde{\zeta}_i - [p]\tilde{\zeta}_m^{[k]}} \right) \right) \\ &\equiv [p]W_{i[k]}^1 \Gamma_1^{[k]} + [p]W_{i[k]}^m \Gamma_m^{[k]}, \end{aligned} \quad (20)$$

where

$$[p]W_{i[k]}^1 = \frac{1}{2\pi} \Im \left(\frac{\tilde{n}_i}{\tilde{\zeta}_i - [p]\tilde{\zeta}_1^{[k]}} \right), [p]W_{i[k]}^m = \frac{1}{2\pi} \Im \left(\frac{\tilde{n}_i}{\tilde{\zeta}_i - [p]\tilde{\zeta}_m^{[k]}} \right), \quad (21)$$

are the influence coefficients. The total normal component of the velocity is obtained by adding all contributions from $2(p - 1)$ wake vortices to get

$$[p]v_i^{\tilde{n}} = \sum_{k=1}^{p-1} \left([p]W_{i[k]}^1 \Gamma_1^{[k]} + [p]W_{i[k]}^m \Gamma_m^{[k]} \right). \quad (22)$$

Equation (15) is now modified to give

$$\sum_{j=1}^m V_{ij}^{\tilde{n}} \Gamma_j + [p]v_i^{\tilde{n}} = V_i^{\tilde{n}}, \quad (23)$$

Notice that for the first step the wake is absent and ${}^{[1]}v_i^{\vec{n}} = 0$. The conservation of the vortices involves the entire bound and wake vortices and is given by

$$\sum_{j=1}^m \Gamma_j^{[p]} + \sum_{k=1}^{p-1} \left(\Gamma_1^{[k]} + \Gamma_m^{[k]} \right) = 0. \quad (24)$$

5. Convection of wake vortices, shedding of bound edge vortices and the Kutta condition

A distinctive feature of the discrete vortex method of Belotserkovsky applied to unsteady problems, such as considered in this paper, is that the Kutta condition is not enforced at the LE and TE. Instead the bound vortices at these points are shed regularly at each time step. Right after shedding, the two edges are left with zero vortices, which effectively satisfy the Kutta condition momentarily until the new bound vortices are built up in the next time step. This approach is in contrast to that taken by Ansari et al. (2006a, 2006b) who enforce the Kutta condition at these edges. We have implemented the approach by Ansari et al. and found out, while the trailing edge Kutta condition is seamless, once the leading edge Kutta condition is added the solution breaks down. This is an indication that the Kutta condition in unsteady problems must be treated differently from the steady problems.

In addition to the bound edge vortices that are shed, all wake vortices are convected. Each of these vortices is displaced by the product of the velocity at its location, calculated at the beginning of each time step and the time increment Δt for that time step. Calculation of the velocity at the vortex site is performed using the velocity formula (10). The velocity contributions come from the bound and wake vortices. The effect of its own is excluded in the calculation.

6. Time Marching solution procedure

The time marching solution procedure is outlined using the concepts and formulas introduced so far. Time Step 1 ($t = 0$) :

1. Specify the wing position and velocity.
2. Calculate the bound vortices: $\Gamma_j^{[1]} (j = 1, 2, \dots, m)$

- Non-penetration condition on the wing

$$\sum_{j=1}^m V_{ij}^{\vec{n}} \Gamma_j^{[1]} = V_i^{\vec{n}}, \quad (25)$$

- Conservation of the vortices

$$\sum_{j=1}^m \Gamma_j^{[1]} = 0. \quad (26)$$

3. Calculate induced velocity, $v_1^{[1]}$ and $v_m^{[1]}$, at the LE and TE, $\tilde{\zeta}_1^{[1]}$ and $\tilde{\zeta}_m^{[1]}$.
4. Shed the bound vortices, $\Gamma_1^{[1]}$ and $\Gamma_m^{[1]}$, at the LE and TE and determine the locations, ${}^{[2]}\tilde{\zeta}_1^{[1]}$ and ${}^{[2]}\tilde{\zeta}_m^{[1]}$, according to

$${}^{[2]}\tilde{\zeta}_1^{[1]} = \tilde{\zeta}_1^{[1]} + v_1^{[1]} \Delta t, \quad {}^{[2]}\tilde{\zeta}_m^{[1]} = \tilde{\zeta}_m^{[1]} + v_m^{[1]} \Delta t.$$

Time Step 2 ($t = \Delta t$):

1. Specify the wing position and velocity.
2. Calculate the bound vortices: $\Gamma_j^{[2]}$, ($j = 1, 2, \dots, m$)
 - Non-penetration condition on the wing

$$\sum_{j=1}^m V_{ij}^{\tilde{n}} \Gamma_j^{[2]} + {}^{[2]}v_i^{\tilde{n}} = V_i^{\tilde{n}}, \quad (27)$$

- Conservation of the vortices

$$\sum_{j=1}^m \Gamma_j^{[2]} + \Gamma_1^{[1]} + \Gamma_m^{[1]} = 0. \quad (28)$$

3. Calculate induced velocity, $v_1^{[2]}$ and $v_m^{[2]}$, at the LE and TE, $\tilde{\zeta}_1^{[2]}$ and $\tilde{\zeta}_m^{[2]}$.
4. Shed the bound vortices, $\Gamma_1^{[2]}$ and $\Gamma_m^{[2]}$, at the LE and TE and determine the locations, ${}^{[3]}\tilde{\zeta}_1^{[2]}$ and ${}^{[3]}\tilde{\zeta}_m^{[2]}$, according to

$${}^{[3]}\tilde{\zeta}_1^{[2]} = \tilde{\zeta}_1^{[2]} + v_1^{[2]} \Delta t, \quad {}^{[3]}\tilde{\zeta}_m^{[2]} = \tilde{\zeta}_m^{[2]} + v_m^{[2]} \Delta t.$$

5. Calculate induced velocity, ${}^{[2]}v_1^{[1]}$ and ${}^{[2]}v_m^{[1]}$, at the wake vortices, ${}^{[2]}\tilde{\zeta}_1^{[1]}$ and ${}^{[2]}\tilde{\zeta}_m^{[1]}$.
6. Convect the wake vortices, $\Gamma_1^{[1]}$ and $\Gamma_m^{[1]}$ and determine the locations, ${}^{[3]}\tilde{\zeta}_1^{[1]}$ and ${}^{[3]}\tilde{\zeta}_m^{[1]}$, according to

$${}^{[3]}\tilde{\zeta}_1^{[1]} = {}^{[2]}\tilde{\zeta}_1^{[1]} + {}^{[2]}v_1^{[1]} \Delta t, \quad {}^{[3]}\tilde{\zeta}_m^{[1]} = {}^{[2]}\tilde{\zeta}_m^{[1]} + {}^{[2]}v_m^{[1]} \Delta t.$$

Repeat the processes for Time Step 3, where four wake vortices are present and two new vortices will be shed from the LE and TE. More time steps are followed as required. The selection of the time increment Δt that is consistent with the spacial resolution, determined by the spacing of bound vortices on the wing, is discussed in Appendix 3.

7. Impulses and force/moment

7.1. Space-fixed system

According to Helmholtz's third theorem (Katz & Plotkin, 2001; Ashley & Landahl, 1985) for the inviscid flow, multiple vortices present in 2D must be conserved and its total magnitude remains zero if the problem started with zero vorticity. Each discrete vortex in 2D is a line vortex with an infinite length in the out-of-plane direction. This vortex is not closed. In order to form a closed vortex loop, we need to amend this vortex with another vortex having the circulation of the same magnitude but opposite signs. These two vortices are joined at infinity to form a closed, albeit infinitely long, vortex loop in the extended 3D space.

In the presence of multiple bound and wake vortices, it may not be possible to find out the exact partner of a selected vortex that has the same magnitude of circulation as the original with the opposite sign. However, as long as the sum of the circulation of all vortices is zero, it is always possible to break down the given distribution into an alternative, but equivalent, distribution of vortices consisting of pairs of vortices each with the same magnitude but opposite signs.

We consider a pair of line vortices Γ and $-\Gamma$ (located at $\tilde{\zeta}_1$ and $\tilde{\zeta}_2$, respectively) with the circulation of the same magnitude Γ but opposite signs. The sign of the counterclockwise circulation is positive. The goal is to calculate the impulses induced by this pair onto the air in terms of the velocity potential function (Lamb, 1932). Since the air extends to infinity, the problem becomes unbounded, if a single line vortex is considered. Treating a pair of vortices of the property described above will eliminate this problem. In the derivation, we have used the complex variable potential function (9) for the line vortex. The complex variable linear impact vector for the pair is given (Ansari et al., 2006a; McCune & Tavares, 1993) by

$$\tilde{\mathcal{I}} = -i\rho\Gamma(\tilde{\zeta}_1 - \tilde{\zeta}_2), \quad (29)$$

where ρ is the air density. The angular impulse (a real value) is given (Ansari et al., 2006a; McCune & Tavares, 1993) by

$$\tilde{\mathcal{I}}_A = -\frac{1}{2}\rho\Gamma(|\tilde{\zeta}_1|^2 - |\tilde{\zeta}_2|^2). \quad (30)$$

In the applications, it is possible to assign impulses for individual vortex with the linear $-i\rho\Gamma\tilde{\zeta}$ and angular $-\frac{1}{2}\rho\Gamma|\tilde{\zeta}|^2$ impulses, where Γ is a signed circulation with positive counterclockwise. The time derivatives of the linear and angular impulses will provide the force and moment exerted by the vortex onto the air. It is important to recognise that the force and moment acting on the wing are obtained by reversing the signs of these obtained for the air mass.

7.2. Wing-translating system

Although the linear and angular impulses must be calculated in the space-fixed system, angular momentum around the origin of the space-fixed system

is undesirable in practical applications. Rather, the angular momentum should be calculated about the origin of the wing-translating system, which, for the insect, is where the wing is attached to its body. The problem however is that its origin is not stationary and the formula for the angular momentum obtained by replacing the complex coordinate $\tilde{\zeta}$ with $\hat{\zeta}$ does not represent the real angular impulse. To resolve this issue, we introduce another space-fixed system that has the same origin as the wing-translating system and calculate the angular impulse in this coordinate system. Although this system needs to be updated as the wing-translating system moves on, each one of them in time history is a space-fixed system and is the legitimate system for the calculation of the impulses.

Consider, first, the original space-fixed system $\tilde{O} - \tilde{\xi}\tilde{\eta}$ and the wing-translating system $\hat{O} - \hat{\xi}\hat{\eta}$. The transformation between the two systems is given by

$$\tilde{\zeta} = r + \hat{\zeta}, \quad (31)$$

where $r = L - Ut + i(H - Vt)$. Substitute this relation into Equations (29) and (30) and simplify to get

$$\tilde{\mathcal{I}} = \hat{\mathcal{I}}, \quad \tilde{\mathcal{I}}_A = \hat{\mathcal{I}}_A + \Im(\bar{r}\hat{\mathcal{I}}), \quad (32)$$

where

$$\hat{\mathcal{I}} = -i\rho\Gamma\hat{\zeta}, \quad \hat{\mathcal{I}}_A = -\frac{1}{2}\rho\Gamma|\hat{\zeta}|^2. \quad (33)$$

Now take the time derivative in Equation (32) to get the force and moment,

$$\tilde{\mathcal{F}} = \dot{\tilde{\mathcal{I}}} = \dot{\hat{\mathcal{I}}}, \quad \tilde{\mathcal{M}} = \dot{\tilde{\mathcal{I}}}_A = \dot{\hat{\mathcal{I}}}_A + \Im(\dot{\bar{r}}\hat{\mathcal{I}}) + \Im(\bar{r}\dot{\hat{\mathcal{I}}}) \quad (34)$$

At this point we switch from the original space-fixed system to the much talked about space-fixed system that is placed on top of the wing-translating system, for which $r = 0$, giving the updated relations

$$\tilde{\mathcal{F}} = \dot{\tilde{\mathcal{I}}} = \dot{\hat{\mathcal{I}}}, \quad \tilde{\mathcal{M}} = \dot{\tilde{\mathcal{I}}}_A = \dot{\hat{\mathcal{I}}}_A + \Im(\dot{\bar{r}}\hat{\mathcal{I}}), \quad (35)$$

where $\dot{\bar{r}} = \dot{L} - U - i(\dot{H} - V)$ is the conjugate complex velocity of the coordinate origin \hat{O} of the wing-translating system. The force and moment acting on the wing are obtained by reversing the signs.

The force and moment in 2D are calculated per unit depth in the out-of-plane direction. Consider an insect with the span length l . In 3D, the wing undergoes a radial flapping motion about the wing base. In 2D adaptation of this flapping motion, we determine its stroke line length d by projecting the 3D flapping motion of the mid-point at $0.5l$ rather than the wing tip, at l of the wing, in order to represent the average (over the span) stroke line length of the 3D flapping wing.

Note that, the program inputs the half span length $0.5l$ and obtains the force and moment per unit span length. The total force and moment are calculated by

Table 1. Flight parameters for the crane fly.

Translational velocity	$U = 100 \text{ cm/s}, V = 0 \text{ cm/s}$
Span and chord lengths	$l = 1 \text{ cm}, c = 0.5 \text{ cm}$
Top and bottom stroke angles	$\phi_T = 30^\circ, \phi_B = -90^\circ$
Stroke line angle	$0^\circ \leq \beta < 90^\circ$
Flapping frequency	$f = 50 \text{ Hz}$
Pitching speed, amplitude, offset	$p = 5, 45^\circ, 0$
Pitch axis offset	$a = 0 \text{ cm}$

multiplying the span length l . For two wings, on the right and left, we further double the total force and moment.

8. Evaluation of numerical performance

8.1. Effect of the spacial and time resolution

The spacial resolution is determined by the number of equally spaced bound vortices, m_0 , which determines the spacing between bound vortices. As described in Appendix 3, m_0 vortices are, originally, placed at an equal interval, which is refined by adding four more vortices near the two ends of the wing to make the total $m = m_0 + 4$.

The minimum number of bound vortices is three ($m_0 = 3$), one each at the LE and TE and one at the middle of the wing. Once the spacial resolution is specified by m_0 , the first candidate for the time increment is determined in terms of m_0 and the stroke line length d ; this time increment depends on the heave motion (Appendix 3) and denoted by Δt_d . Another time increment Δt_p is determined by the pitch speed p (Appendix 1). The smaller of the two is used for the actual time increment. The time increment used is nondimensionalised by the half-period of flapping. Notice that m_0 is the only non-physical parameter that can be selected independently from all other physical parameters, including d and p , that define the problem.

Figure 5 shows the variation of lift and drag forces for a single period for various values of m_0 in a combined flapping (heave and lunge) and rotation (pitching). The input parameters are obtained from the flight data of a crane fly and are given by Table 1 with the stroke line angle $\beta = 10^\circ$. The nondimensional time increment determined by Equation (C1), using the parameters from Table 1, is $\Delta t_d = 0.267/(m_0 - 1)$. The time increment determined by the pitch using Equation (C3) with $p = 5$ and $r_p = 0.1$ gives $\Delta t_p = 0.08$. Figure 5(a) shows the lift force, for a period, for $m_0 = 3, 5, 10, 15, 20$ and Figure 5(b) shows the lift force for $m_0 = 20, 25, 30, 35$. The corresponding drag force is plotted in Figures 5(c) and (d). For both groups of m_0 , except for $m_0 = 3$, the time increment is determined by Δt_d (lunge and heave time increment). This is because the speed of pitch is slow. Notice that the solution jumps quickly for the first small values of m_0 as we increase m_0 , but the rate of change slows down after $m_0 = 20$. Whether the solution converges to the correct solution as we increase m_0 is

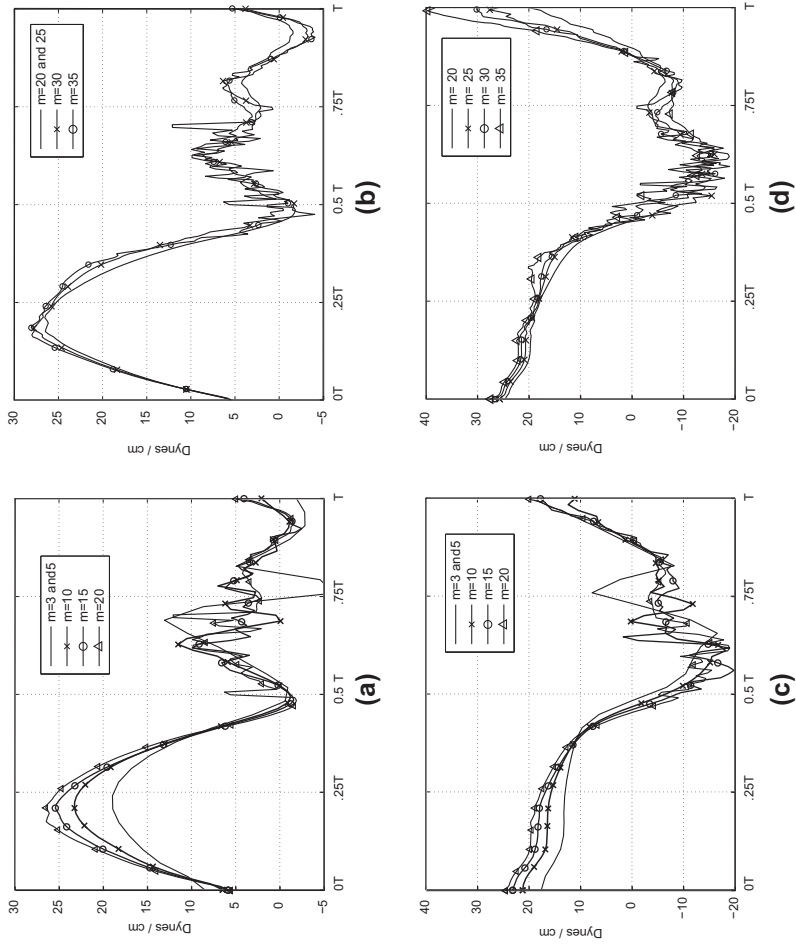


Figure 5. Lift/Drag force variation (dyne/cm) for a single period for various values of m_0 . (a) Lift force for $m_0 = 3, 5, 10, 15, 20$, (b) for $m_0 = 20, 25, 30, 35$. (c) Drag force for $m_0 = 3, 5, 10, 15, 20$, (d) for $m_0 = 20, 25, 30, 35$.

Table 2. Parameters for pure heave. See Figure 6.

Translational velocity	$U = 20 \text{ cm/s}, V = 0 \text{ cm/s}$
Span and chord lengths	$l = 2000 \text{ cm}, c = 100 \text{ cm}$
Top and bottom stroke angles	$\phi_T = 5.739^\circ, \phi_B = -5.739^\circ$
Stroke line angle	90°
Flapping frequency	$f = 0.028 \text{ Hz}$
Pitching speed, amplitude, offset	$p = 30, 0^\circ, 0$
Pitch axis offset	$a = 0 \text{ cm}$

Table 3. Parameters for combined heave and pitch. See Figure 7.

Translational velocity	$U = 20 \text{ cm/s}, V = 0 \text{ cm/s}$
Span and chord lengths	$l = 2000 \text{ cm}, c = 100 \text{ cm}$
Top and bottom stroke angles	$\phi_T = 5.739^\circ, \phi_B = -5.739^\circ$
Stroke line angle	90°
Flapping frequency	$f = 0.028 \text{ Hz}$
Pitching speed, amplitude, offset	$p = 30, 19.27^\circ, 0$
Pitch axis offset	$a = 0 \text{ cm}$

Table 4. Computing time comparison for the VM and OpenFOAM. See Figures 6 and 7.

Problem	VM ($m_0=15$) (S)	VM ($m_0=35$) (S)	OpenFOAM (S)
pure heave	166.8	183.6	3300
heave and pitch	177	186.6	3468

answered below in comparison with the solution obtained by a Navier–Stokes solver, OpenFOAM (Weller, Tabor, Jasak, & Fureby, 1998).

8.2. Comparison with results obtained by a Navier–Stokes solver

After studying the effects of m_0 in the previous subsection, we need to verify if the solution converges to the more accurate reference solution as we increase m_0 . We have used a Navier–Stokes solver, OpenFOAM, to provide such a reference. Figure 6(a) shows comparison of drag and lift forces for pure heave obtained by our vortex method, with $m_0 = 15$ and $m_0 = 35$, and OpenFOAM. The flight parameters are given by Table 2. The time increment determined by the heave only, using the data in Table 2 and Equation (C1), is given by $\Delta t_d = 0.5/(m_0 - 1)$. Figure 6(b) shows the corresponding vortex fields produced by two methods. The values $m_0 = 15$ and $m_0 = 35$ give the results that best fit to the OpenFOAM solution among other values tried as described below.

Next, Figure 7(a) shows the comparison of the heave and pitch combination obtained by two methods with the flight parameters for the vortex method given by Table 3. The time increment based on the heave is the same as above and the time increment for pitching, with $p = 30$ and $r_p = 0.1$, is $\Delta t_p = 1/75 \sim 0.0133$. The comparison of the corresponding vortex fields is given in Figure 7(b). The number of m_0 used in the vortex method is $m_0 = 15$ and $m_0 = 35$ for this case also, which give the best fit to the OpenFOAM solution. The time increment is determined by the pitch time increment Δt_p .

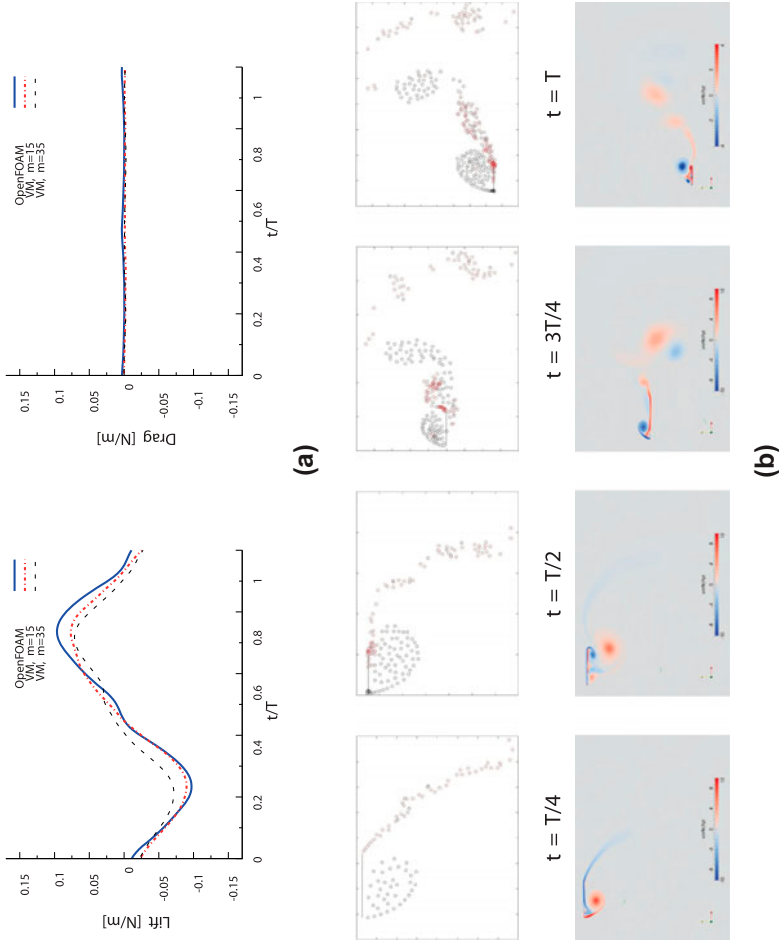


Figure 6. (a) Comparison of lift and drag forces for pure heave obtained by the vortex method (VM) and OpenFOAM, (b) Corresponding vortex fields by the vortex method (top) and OpenFOAM (bottom).

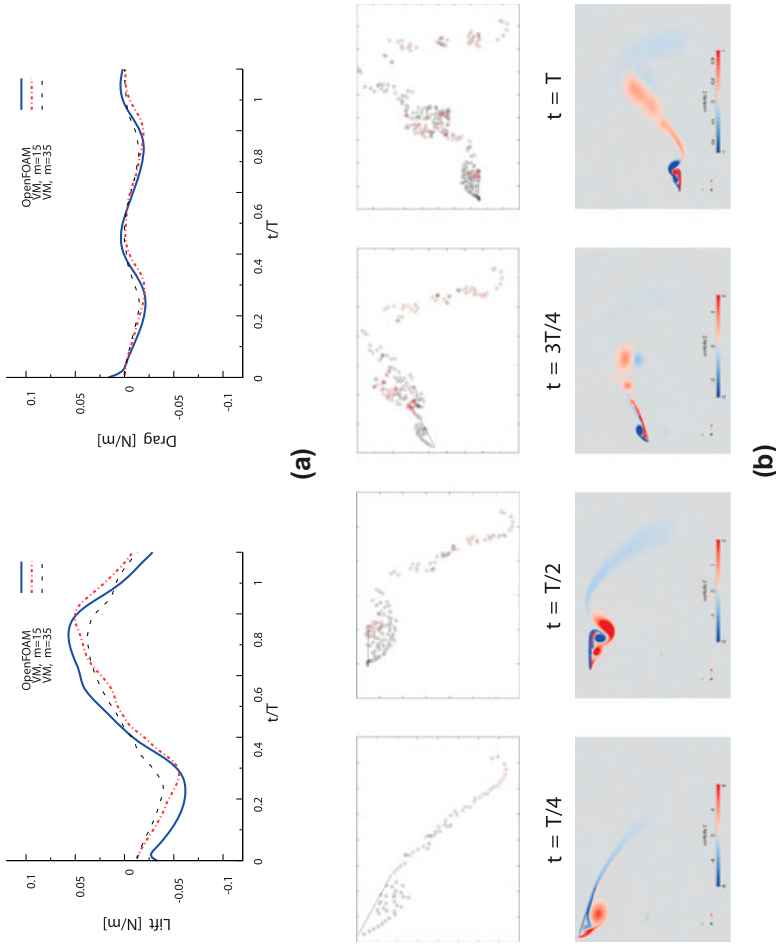


Figure 7. (a) Comparison of lift and drag forces for combined heave and pitch obtained by the vortex method and OpenFOAM, (b) Corresponding vortex fields by the vortex method (top) and OpenFOAM (bottom).

Table 4 shows the comparison of time required to calculate the two problems by the two methods. For two cases above, the OpenFOAM simulations were performed in parallel on 6 cores, while the vortex method simulation on 1 core. For both $m_0 = 15$ and $m_0 = 35$, the speed up is approximately 20 in favour of the vortex method. During the simulation, we have used different values of m_0 . As we increased the number of m_0 , the solution has improved rapidly for $m_0 = 3, 5, 10, 15, 20$. The solution stabilised and approached towards the OpenFOAM solution around $m_0 = 20, 25, 30, 35$, but began to deviate from the OpenFOAM solution after $m_0 = 35$. The important lesson is that the solution does not seem to converge to the viscous solution as we increase the value of m_0 . For a large number of m_0 , the wake is packed with vortices and, unless special techniques such as lumping nearby vortices or allowing vortex decay, numerical difficulties are expected even with the use of the Rankine vortex designed to avoid this problem. Rather than attempting to achieve the convergence to the reference solution obtained by the Navier–Stokes solver, it would be wise to know the limit of the present method and use it in the range that gives the optimum results.

Finally, the Reynolds number in the OpenFOAM calculation was very low at 1,100 to make sure the flow is laminar. Note that the vortex method proposed here is based on the inviscid flow theory and does not involve the Reynolds number.

8.3. Optimum number of m_0

Our surprising discovery is that, although the results using a small number of m_0 is quantitatively inferior, they still preserve the essence of the solution, obtained using a much higher number of m_0 qualitatively. We have found that for the value of m_0 bigger than 35, the computational time increases exponentially but the numerical results deteriorate as compared to the viscous solution obtained by a Navier–Stokes solver. Although more numerical study on the influence of m_0 coupled with p is required, the optimum number of m_0 , determined by the accuracy and the computation time, found so far is around 35.

The above observation on the method gives us the best use of the proposed method as a quick solver for the unsteady flapping problems. Using a small number of m_0 , such as $m_0 = 5$ and $m_0 = 10$, we can explore the unknown unsteady behaviour of the flapping flight. Once we discover interesting phenomena or behaviours, we can increase the number of m_0 (up to $m_0 = 35$) for more accurate results. If the phenomena need to be further scrutinised, then we switch onto one of the Navier–Stokes solvers. We can remain confident that use of this method with a small number of m_0 does not miss the essential behaviour and is quick to calculate. The method is also useful in the design process of the MAVs.

9. Insect flight analysis example

We have analysed the crane fly flight using the proposed vortex method to find out if the method can predict the enough lift force to support the weight of a

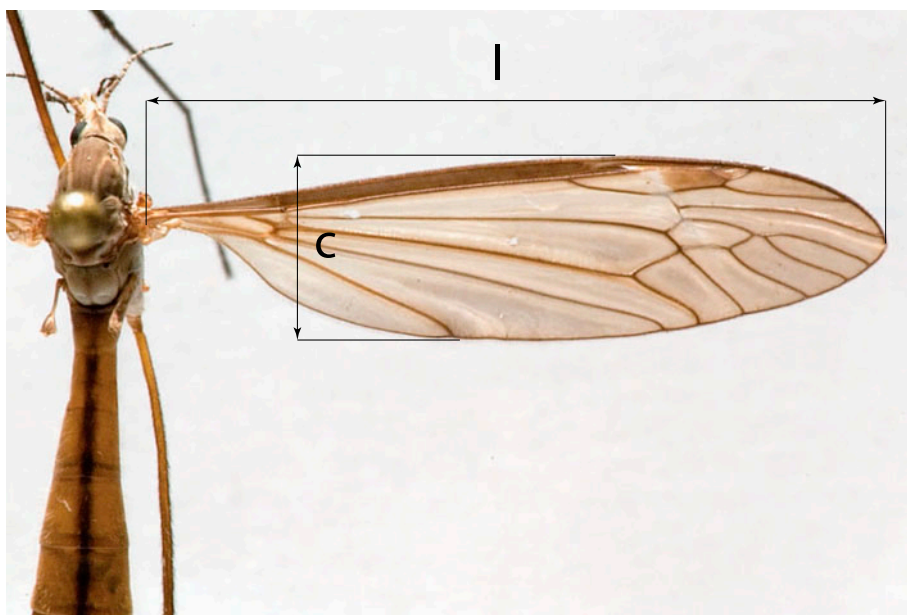


Figure 8. Crane fly with its wing span l and chord length c .

crane fly. The picture of a crane fly is shown in Figure 8 and its flight parameters in Table 1. The motion parameters are taken from the high-speed Movie 1 (Supplemental online material) of the crane fly in tethered flight, except for the stroke line angle. Due to the constraint in the tethered flight, the stroke line angle was not determined reliably. Therefore, we opted to vary the stroke line angle, in the analysis, to determine the stroke line angle that gives the best lift force. Figure 9(b) shows the variation of the lift force for a single period for various values of stroke line angle β between 0° and 90° . The average (over the period) lift force for each stroke line angle is shown in Figure 9(a). We have found that the best lift force is obtained for the stroke line angle $\beta = 10^\circ$ (Figure 9(c)) and the worst at 90° (Figure 9(d)). Notice that the best stroke line angle is close to the angle observed in a natural flight movie, Movie 2 (Supplemental online material). The average (over a period) lift force for $\beta = 10^\circ$ is 11 dyne per unit depth of 1 cm. Multiply this by the span length of 2 cm and doubling the product, for two wings, will give 44 dyne of lift force. This exceeds the weight of a crane fly, 30 dyne. The value of $m_0 = 35$ was used in the analysis.

Next example is the flight of the honey bee in hover. The flight parameters, except for the stroke line angle, for the honey bee were taken from the high-speed Movie 3 (Supplemental online material) of the honey bee and listed in Table 5. The analysis was performed with various stroke line angles to determine the best stroke line angle to produce the maximum lift. Figure 10(b) shows the variation of the lift force for a single period for various values of stroke line angle β between -80° and 80° for the honey bee in hovering ($U = 0$ cm/s). The average (over

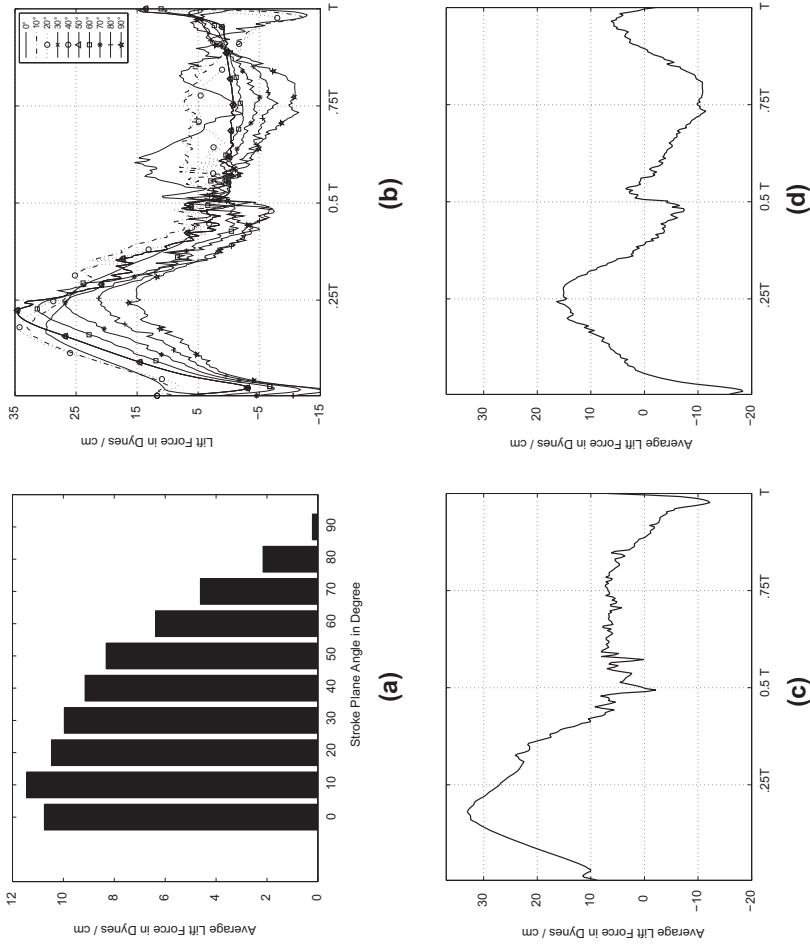


Figure 9. (a) The average lift force (over the period) for various stroke line angles β for the crane fly. (b) The corresponding variations of the lift force over a period, (c) with the best case ($\beta = 10^\circ$) and (d) and the worst case $\beta = 90^\circ$.

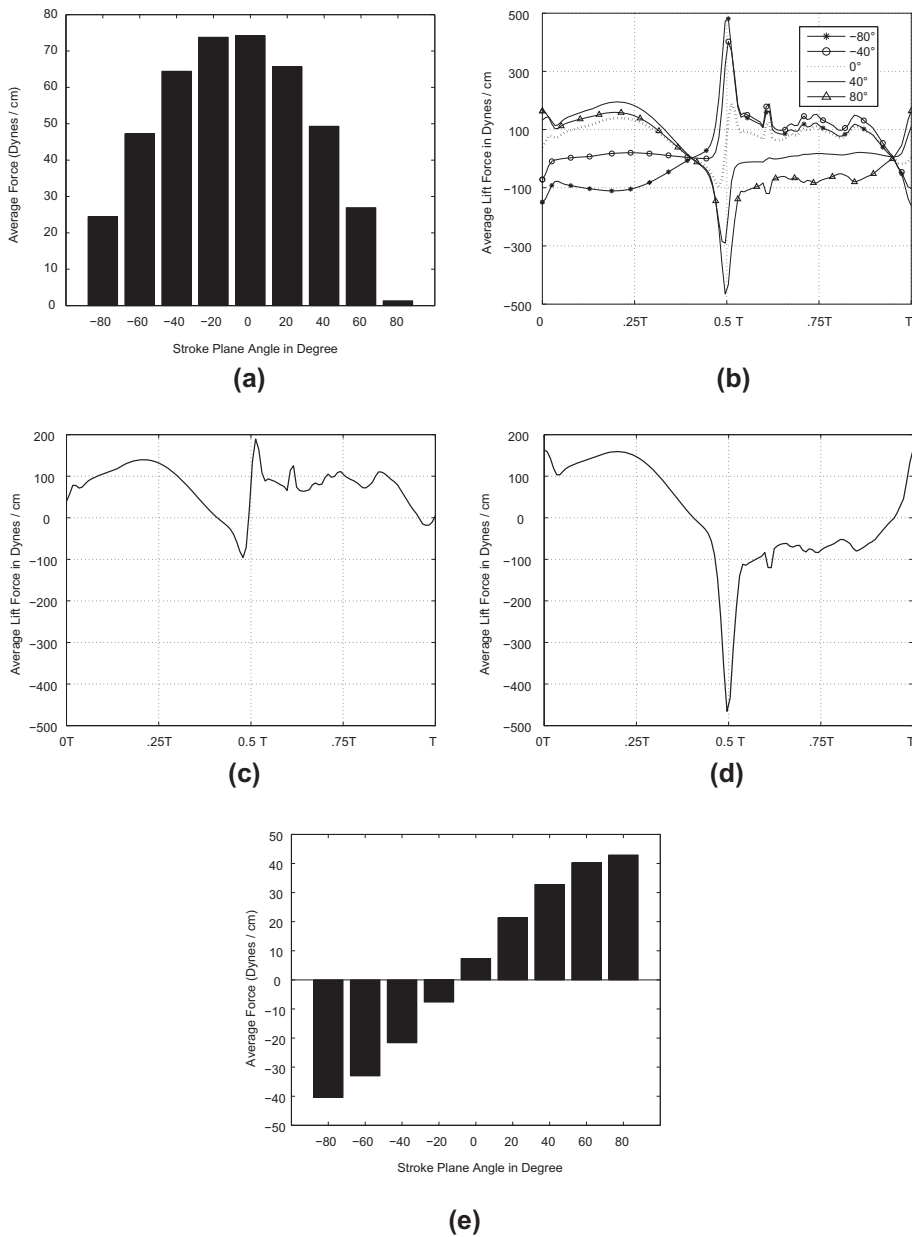


Figure 10. (a) The average lift force (over the period) for various stroke line angles β for the honey bee. (b) The corresponding variations of the lift force over a period, (c) with the best case ($\beta = 0^\circ$) and (d) and the worst case $\beta = 80^\circ$. (e) The average drag force (over the period) for various stroke line angles β .

the period) lift force for each stroke line angle is shown in Figure 10(a). We have found that the best lift force is obtained for the stroke line angle $\beta = 0^\circ$ (Figure 10(c)) and the worst at 80° (Figure 9(d)). The average (over a period) lift force for β between -40° and $+40^\circ$ produces more than 60 dyne per unit depth of

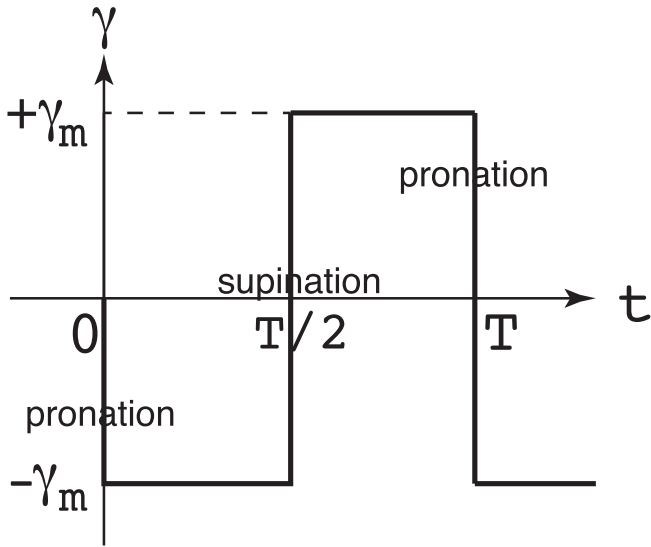


Figure 11. Perfect pronation and supination.

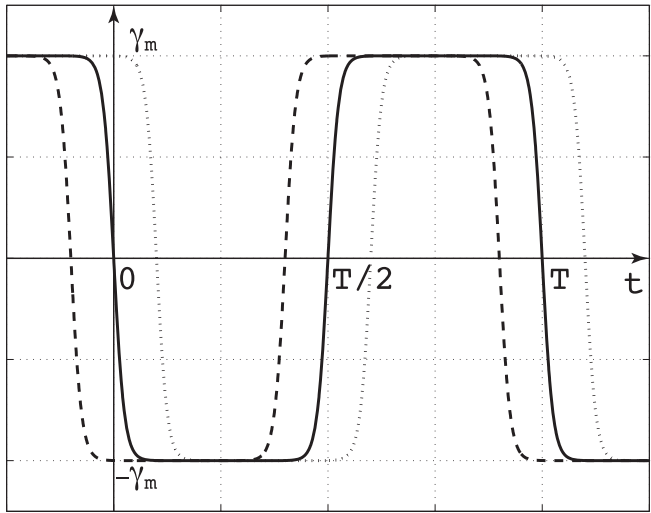


Figure 12. Smoothed pitch motion with symmetric (solid), advanced (dashed) and delayed (dotted) pitch.

1 cm. Multiply this by the span length of 1.2 cm and doubling the product, for two wings, will give 144 dyne of lift force. This exceeds the weight of a honey bee, 120 dyne. The value of $m_0 = 35$ was used in the analysis.

Figure 10(e) shows the variation of the average drag force. Notice that for the positive stroke line angle, thrust (and impending forward motion) is produced, while for the negative stroke line angle, drag (and impending backward motion) is produced. According to [Wigglesworth \(1972\)](#), the honey bee in hovering flight

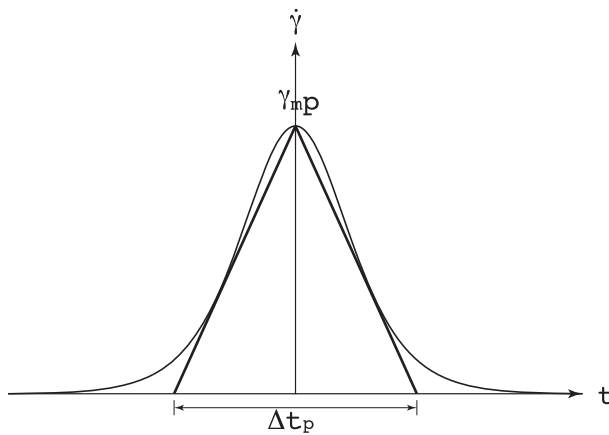


Figure 13. Approximate pitch velocity variation.

Table 5. Flight parameters for the honey bee.

Translational velocity	$U = 0 \text{ cm/s}, V = 0 \text{ cm/s}$
Span and chord lengths	$l = 1.2 \text{ cm}, c = 0.5 \text{ cm}$
Top and bottom stroke angles	$\phi_T = 70^\circ, \phi_B = -30^\circ$
Stroke line angle	$-80^\circ \leq \beta < +80^\circ$
Flapping frequency	$f = 200 \text{ Hz}$
Pitching speed, amplitude, offset	$p = 20, 45^\circ, 0$
Pitch axis offset	$a = 0 \text{ cm}$

increases its stroke line angle to start the forward motion and decreases the angle in the backward motion. He also describes the increase in the lift force as the stroke line angle decreases. Our analysis has verified these observations.

10. Concluding remarks

Despite the myth that the inviscid fluid theory cannot deal with the unsteady viscous problems, numerical results obtained from the analysis suggest that this method can predict the unsteady phenomena reliably through comparisons with numerical results obtained using a more precise Navier–Stokes solver. The main advantage is the remarkably less time required to solve the problems compared to Navier–Stokes solvers. It should be warned that the method proposed, however, does not replace the more elaborate and accurate, albeit time-consuming, solutions by Navier–Stokes solvers. The method, instead, is best used for getting the quick estimate of unsteady flapping flight of insects flight without missing the essence of the unsteady phenomena involved. The proposed method provides an affordable tool in the exploration of yet unknown world of unsteady flapping dynamics to discover and identify new effects and phenomena. Once such discoveries are made, we can always turn on the more advanced, albeit expensive, Navier–Stokes solvers for more precise scientific investigation. The proposed method also provides an affordable tool in the design of MAVs.

In this paper, the wings are assumed rigid and straight. However, the wings of real insects are flexible and curved or cambered. The introduction of the camber is straightforward within the framework of the rigid wing. All we need is to specify, in Section 2.3, the camber by the function $\eta = f(\xi)$ and derive the equations for the unit normal and normal velocity for the curved wing. The effects of the motion-induced wing deformation are more difficult to accommodate and the full fluid–structure interaction problem must be addressed. To make the matter more complex, the deformation is large and the nonlinear treatment is required.

The proposed method can readily be extended to multiple wing problems in 2D to analyse the flight of dragonflies and lacewings. The main issue there will be the effect of the synchronisation of the wing motion of forward and hind wings.

Yet, another direction for future study is the extension of the current approach to 3D. Instead of the infinite vortex lines in 2D, vortex rings must be used in 3D. For each iteration step, a single vortex ring is shed from the bounding edge of the 3D wing.

The ultimate goal of the current line of work is to develop the flight simulator for insect flapping flight in 3D. For that purpose, six degrees of freedom equations of motion consisting of the Newton and Euler equations must be developed based on the input force generated by the fluid analysis code with the possible inclusion of the effects of wing deformation generated by the structural analysis code.

Disclosure statement

No potential conflict of interest was reported by the authors.

ORCID

M. Denda  <http://orcid.org/0000-0001-9652-3540>

Pruthvi K. Jujjavarapu  <http://orcid.org/0000-0002-7280-5110>

Brandon C. Jones  <http://orcid.org/0000-0002-9352-5521>

References

- Acheson, D. J. (1990). *Elementary fluid dynamics*. Oxford: Oxford University Press.
- Ansari, S. A., Zbikowski, R., & Knowles, K. (2006a). Non-linear unsteady aerodynamic model for insect-like flapping wings in the hover. Part 1: Methodology and analysis. *Proceedings of the Institution of Mechanical Engineers, Part G: Journal of Aerospace Engineering*, 220(G2), 61–83.
- Ansari, S. A., Zbikowski, R., & Knowles, K. (2006b). Non-linear unsteady aerodynamic model for insect-like flapping wings in the hover. Part 2: Implementation and validation. *Proceedings of the Institution of Mechanical Engineers, Part G: Journal of Aerospace Engineering*, 220(G2), 169–186.
- Ashley, H., & Landahl, M. (1985). *Aerodynamics of wings and bodies*. New York, NY: Dover Publications.
- Belotserkovsky, S. M., Kotovskii, V. N., Nisht, M. I., & Fedorov, R. M. (1993). *Two-dimensional separated flows*. Boca Raton FL: CRC Press.
- Belotserkovsky, S. M., & Lifanov, I. K. (2003). *Methods of discrete vortices*. Boca Raton FL: CRC Press.

- Katz, L., & Plotkin, A. (2001). *Low-speed aerodynamics*. Cambridge: Cambridge University Press.
- Lamb, S. H. (1932). *Hydrodynamics* (6th ed.). Cambridge: Cambridge University Press.
- Lewis, R. I. (1991). *Vortex element methods for fluid dynamic analysis of engineering systems*. Cambridge: Cambridge University Press.
- Liu, H., & Aono, H. (2009). Size effects on insect hovering aerodynamics: An integrated computational study. *Bioinspiration & BioMimetics*, 4, 015002.
- McCune, J. E., & Tavares, T. S. (1993). Perspective: Unsteady wing theory – The Kármán/sears legacy. *The Journal of Fluids Engineering*, 115, 548–560.
- Sears, W. R. (2011). *Introduction to theoretical aerodynamics and hydrodynamics*. Reston, VA: AIAA.
- von Kármán, T., & Sears, W. R. (1938). Airfoil theory for non-uniform motion. *Journal of the Aeronautical Sciences*, 5, 379–390.
- Wang, Z. J. (2005). Dissecting insect flight. *The Annual Review of Fluid Mechanics*, 37, 183–210.
- Weller, H. G., Tabor, G., Jasak, H., & Fureby, C. (1998). A tensorial approach to computational continuum mechanics using object-oriented techniques. *Computers in Physics*, 12, 620–631.
- Wigglesworth, V. B. (1972). *The principles of insect physiology*. London: Chapman and Hall.

Appendix 1. Wing motion

A.1. Lunge and heave

Using the hypothetical wing length $0.5l$ and top and bottom stroke angles ϕ_T and ϕ_B , we can calculate the stroke line length

$$d = d_T + d_B, \quad (\text{A1})$$

where $d_T = 0.5l \sin(\phi_T)$ and $d_B = 0.5l \sin(-\phi_B)$, the minus sign is required since the default sign for ϕ_B is negative. The origin \hat{O} of the wing-translating system is located on the stroke line and moves along it. Its global position is given by $(L - Ut, H - Vt)$, in terms of the heave H , lunge L and the ambient air velocity components, U and V . The lunge and heave are described by the sinusoidal function

$$L = \frac{1}{2} \left(d \cos \frac{2\pi(t + \tau)}{T} + e \right) \cos \beta, \quad (\text{A2})$$

$$H = \frac{1}{2} \left(d \cos \frac{2\pi(t + \tau)}{T} + e \right) \sin \beta, \quad (\text{A3})$$

where $e = d_T - d_B$ is the stroke length difference parameter between the top and bottom strokes, τ and T are the phase shift and the period of motion and β is the stroke line angle. When $\tau = 0$, the motion starts from the top, while for $\tau = T/2$ the motion starts from the bottom. By varying the phase shift, between 0 and T , we can produce sinusoidal motions with various starting positions. The rates of lunge and heave are obtained by the time derivatives

$$\dot{L} = -\frac{\pi d}{T} \sin \frac{2\pi(t + \tau)}{T} \cos \beta, \quad (\text{A4})$$

$$\dot{H} = -\frac{\pi d}{T} \sin \frac{2\pi(t + \tau)}{T} \sin \beta. \quad (\text{A5})$$

A.2. Pitch (Rotation)

The rotation (pitch) γ of the wing occurs around the origin \hat{O} of the wing-translating system, as shown in Figure 2. It is positive clockwise. Without the pitch, the wing chord line remains perpendicular to the stroke line. With a non-zero pitch γ , the attack angle of the chord line

is given by $\alpha = \pi/2 - (\beta - \gamma)$. The perfect pitch occurs instantaneously at the ends of the down and up strokes; pronation at the top and supination at the bottom of the stroke. While each sudden pitch is described by a step function, the periodic series of pronations and supinations are described by a superposition of the step functions as shown in Figure 11, which corresponds to the lunge and heave motion (A2) with $\tau = 0$. If the perfect pitch occurs exactly at the top or bottom of the stroke, then it is called symmetrical pitch. The timing of the pitch can be either before the top or bottom (advanced pitch) or after them (delayed pitch). These timings are specified by a timing offset parameter μ .

Actual insects can never achieve the perfect pitch, rather the pitch motion is smoothed significantly. This smoothed pitch motion is conveniently described by the function

$$f_{t_i} = \frac{2}{1 + e^{-2p(t-t_i)}}, \quad (\text{A6})$$

which describes the step function that jumps from 0 to 1 at $t = t_i$ when $p \rightarrow \infty$. Each supination and pronation is obtained using the amplitudes $+2\gamma_m$ and $-2\gamma_m$, respectively. The entire series of smooth pitching in one period is given by the superposed smooth step functions by

$$\gamma = \gamma_m(1 - f_0 + f_{T/2} - f_T). \quad (\text{A7})$$

Figure 12 shows variations of smooth pitching with symmetric, advanced and delayed pitching.

The pitch rate is obtained by the time derivative

$$\dot{f}_{t_i} = \frac{4pe^{-2p(t-t_i)}}{(1 + e^{-2p(t-t_i)})^2}, \quad (\text{A8})$$

in

$$\dot{\gamma} = \gamma_m(-\dot{f}_0 + \dot{f}_{T/2} - \dot{f}_T). \quad (\text{A9})$$

If the timing of the pitch is offset, then replace t_i above by $t_i + \mu$, where $\mu < 0$ for advanced and $\mu > 0$ for delayed pitch.

A.3. Physical meaning of pitch parameter p

Let Δt_p be the time the approximate step function f_{t_i} takes to complete the smooth increase of pitch by the amount $2\gamma_m$. The velocity variation has a bell shape, as shown in Figure 13, and its maximum value that occurs at $t = t_i$ is calculated, from Equation (A8), to be $\gamma_m p$. Replace the bell-shaped velocity distribution by an inscribing triangle with base length Δt_p and the height $\gamma_m p$. The average velocity over this period is calculated to be $1/2\gamma_m p$, which is multiplied by Δt_p to produce the total jump $2\gamma_m$. This process will produce a relation

$$p = \frac{4}{\Delta t_p}. \quad (\text{A10})$$

This is a key relation that gives the physical interpretation of the parameter p . Since the maximum transition time for the pitch is half period, $(\Delta t_p)_{\max} = T/2$, the minimum value of the pitch parameter is $p_{\min} = 8/T$. This gives the slowest pitch motion we can achieve and it looks almost like a portion of the sinusoidal function. The estimation here is approximate since the bell-shaped velocity variation is replaced by a triangle and the base length of the inscribing triangle, $(\Delta t_p)_{\max}$, can never reach the maximum value $T/2$. Therefore, the minimum value of p needs to be set at slightly higher than $8/T$.

Appendix 2. Rankine vortex

As the distance r between the observation and vortex points approaches zero, the velocity at the observation point is unbounded. This tendency becomes prevalent when the number of wake vortices increases. In order to avoid excessive magnitude of velocity, we introduce a vortex core model such that the velocity within the vortex core of radius r_c is made to decrease linearly to zero from the value taken at the outer boundary of the circular vortex core. Let $\tilde{\zeta}$ and $\tilde{\zeta}_0$ be the observation and vortex points, respectively. The conjugate of the complex velocity at $\tilde{\zeta}$ is given by the standard formula,

$$\overline{v(\tilde{\zeta})} = -\frac{i\Gamma}{2\pi} \frac{1}{\tilde{\zeta} - \tilde{\zeta}_0}, \quad (\text{B1})$$

for $r = |\tilde{\zeta} - \tilde{\zeta}_0| \geq r_c$. It is shown the corresponding complex conjugate velocity within the vortex core is given by

$$\overline{v(\tilde{\zeta})} = -\frac{i\Gamma}{2\pi} \frac{1}{\tilde{\zeta} - \tilde{\zeta}_0} \left(\frac{r}{r_c}\right)^2, \quad (\text{B2})$$

for $r = |\tilde{\zeta} - \tilde{\zeta}_0| \leq r_c$.

We propose that the vortex core radius r_c is given by the distance between a vortex point and its closest collocation point, which is

$$r_c = 0.5 \frac{c}{m_0 - 1}, \quad (\text{B3})$$

where c is the chord length of the wing and m_0 is the number of equally spaced vortex points on the wing (see Appendix 3). This model is called the Rankine vortex (Acheson, 1990).

Appendix 3. Spatial and time increment resolutions

The bound vortices are spaced at an equal distance on the wing, except in the neighbourhood of the LE and TE. After placing m_0 vortices at an equal interval $\delta c = m_0/c$, two vortices, one at each end, are placed at $1/2\delta c$ from the end; here c is the chord length of the wing. In addition, two more vortices, one at each end again, are placed at $1/4\delta c$ from the end. This refinement scheme is similar to that used in fracture mechanics near the crack tips. The actual number of bound vortices is $m = m_0 + 4$. However, when we refer to the number of bound vortices in this paper, with the exception of Sections 3 and 4, we use the original m_0 , which is the number of originally placed vortices at an equal distance. Note that the bound vortex spacing discussed below is δc , which is obtained in terms of m_0 .

This spacing controls the spacial resolution of the problem. If some vortices penetrate the wing or go through the wing, then one may increase m_0 to decrease the bound vortex spacing. This will enforce the non-penetration condition of the flow on the wing by reducing the distance between collocation points.

With decreasing time increments, further details of the vortex movement are revealed. But how small the time increment should be, given the spacial resolution? To answer this question, we select the non-dimensional time increment to be

$$\Delta t_d = \frac{c}{d} \frac{1}{m_0 - 1}, \quad (\text{C1})$$

where c and d are the chord and stroke line lengths, respectively. In order to justify this selection of time increment, imagine a simple heaving motion of the wing with the stroke line length of d . First, we select the non-dimensional time to cover the stroke line length to be 1. Thus, during a non-dimensional time increment Δt_d , the wing heaves by $d * \Delta t_d$,

which gives the spacial resolution in the vertical direction. While the spacial resolution in the horizontal wing direction is given by $c/(m_0 - 1)$. By equating the spacial resolutions in two directions, we get $d * \Delta t_d = c/(m_0 - 1)$, which gives (C1). This time increment is called heave time increment since it is determined by the heave motion.

In addition, since the non-dimensional duration of pitch (rotation) is given, from (A10), by

$$\Delta t_p^* = \frac{4}{p}, \quad (\text{C2})$$

it is necessary to select the time increment Δt much smaller than Δt_p ,

$$\Delta t_p = r_p \Delta t_p^*, \quad (0 < r_p < 1) \quad (\text{C3})$$

in order to capture the beginning, middle and the end of rotation. The optimum size of r_p to properly capture the rotation will be around 0.1. This time increment is called pitch time increment. Finally, select the minimum of (C1) and (C3) for the time increment of the analysis.